Surface vibrational Raman modes of In:Si(111)(4 × 1) and (8 × 2) nanowires

E. Speiser and N. Esser

Leibniz-Institut für Analytische Wissenschaften-ISAS-e.V, Department Berlin, Schwarzschildstraße 8, 12489 Berlin, Germany

S. Wippermann

*Interface Chemistry and Surface Engineering Department, Max-Planck-Institut für Eisenforschung GmbH, Max-Planck-Straße 1,
40237 Düsseldorf, Germany*

W. G. Schmidt

Lehrstuhl für Theoretische Physik, Universität Paderborn, 33095 Paderborn, Germany

High-resolution Raman spectroscopy at low frequencies (<100 cm^{-1}) is used to reinvestigate and identify the surface phonons localized in the first atomic layers of In:Si(111)(4 × 1) and (8 × 2). The frequency and symmetry of low-energy surface phonons are strongly related to surface structure. The measured phonons are assigned to characteristic modes of the quasi-one-dimensional indium nanowires on Si(111) by means of density-functional theory calculations and symmetry considerations. It is found that the low-temperature (8 × 2) and the room-temperature (4 × 1) phases of the In:Si(111) surface are characterized by distinct sets of phonon modes. Strong modifications in Raman spectra upon the phase transition are, on the one hand, related to backfolding induced by symmetric quadruplication of the surface unit cell and, on the other hand, to structural changes within the surface unit cell. These are indications for two distinct structural phases, supporting the first-order transition scenario. The characteristic structural changes are thus verified in detail.

I. INTRODUCTION

The search for one-dimensional (1D) electronic systems among metallic submonolayer coverages on semiconductor surfaces [1–3] has produced a few prominent examples, one of which is the ordered array of In nanowires on Si(111) surfaces [4,5]. In the past years a commonly accepted structural model has been established by experiment and theory for the In nanowire room-temperature (RT) phase [6–14]. It consists of two In zigzag chains ordered in a (4 × 1) periodicity that are separated by Si chains resembling the π-bonded chains of the clean Si(111)(2 × 1) surface. When the system is cooled below about 120 K the In atoms slightly rearrange and—instead of zigzag chains within a (4 × 1) symmetry—a (8 × 2) surface periodicity is clearly observed with scanning tunneling microscopy [15–20]. The atomic structure of this low-temperature (LT) phase seemed elusive for a long time. Eventually, based on density-functional calculations, a structural model based on In hexagons [21,22] for the (8 × 2) surface was suggested. While this model was found to account for the high-energy positron diffraction data [23,24] as well as the optical signatures [25] measured for the In nanowires at low temperatures, the nature of the phase transition remained a controversial issue. Some theoretical studies propose the phase transition to be of order-disorder type [7,22,26] and explain the RT phase in terms of dynamic fluctuations between degenerate ground-state structures. Another study supports a first-order phase transition of displacive type between two distinct geometrical structures [27]. The theoretical modeling of the (8 × 2)-(4 × 1) phase transition is complicated by an extraordinary sensitivity of the system with respect to the numerical details and approximations made in the calculations; see, e.g., Refs. [28–31]. The experimental findings have been interpreted in terms of a triple-band Peierls instability

[17], a first-order phase transition [20,32], a second-order phase transition [33], and an insulating phase stabilized by many-body effects [34]. The phase transition can be triggered optically as well as influenced by adatoms and defects [35–39].

The exploration of the In:Si(111) vibrational properties is expected to clarify the nature of the (8 × 2)-(4 × 1) phase transition. On the one hand, there are theoretical predictions of soft phonon modes that are responsible for the phase change [27]. On the other hand, the surface atomic structure is typically strongly related to the vibrational properties. In the case of the present system this has already been exploited to exclude earlier structural models for the LT phase [40]. Raman spectroscopy, which has the benefit of a very high spectral resolution, down to few wave numbers, and a broad spectral range of excitations, has in recent years been successfully applied to probe surface phonons [41–45]. Raman scattering from surface phonons is due to deformation potential scattering involving surface electronic states [46] and allows for studying structure formation on semiconductor surfaces [40,47,48]. Both the Raman frequencies as well as the Raman selection rules are linked to the surface structure and thus valuable to validate different competing structural models.

Earlier calculations [27] find that the In:Si(111) high-energy phonons between about 100 and 480 cm^{-1} arise from Si(111) subsurface vibrational modes. In-related surface phonons have energies below about 100 cm^{-1}. Based on these findings we present here a detailed Raman analysis in the energy range of 10–90 cm^{-1} with high spectral resolution that is accompanied by frozen-phonon calculations for the mode assignment. The Raman spectra were recorded in all four possible polarization configurations to address the surface symmetry. The present data clearly show the existence of distinct, In-localized phonon modes that are characteristic for the (8 × 2) and (4 × 1) phase, respectively, and thus give

075417-1

strong evidence for a first-order phase transition between In hexagon rows at low-temperature and zigzag chains that form above 120 K.

II. METHODOLOGY

The Raman experiments were performed in ultrahigh vacuum (UHV) at a base pressure of 2×10^{-10} mbar. The UHV vessel was equipped with a helium closed-cycle cryostat with integrated direct-current heating, a Knudsen cell for In evaporation, low-energy electron diffraction (LEED), Auger electron spectroscopy (AES), and optical windows. A vicinal Si(111) surface with an offcut of approx. $1°$ towards $[\bar{1}\bar{1}2]$ was used in order to trigger the formation of a single-domain surface. The formation of the single domain (4×1) surface and the (4×1)-(8×2) surface phase transition was monitored *in situ* with reflectance anisotropy spectroscopy (RAS) [49]. RAS measures the difference in reflectance, at near normal incidence, of light linearly polarized in two orthogonal directions at the surface plane of a cubic material. With a three-domain surface of equal statistical weight, no anisotropy would be observed because of domain averaging. Consequently, the amplitude of the RAS signal is maximum if the surface is single domain [49]. For the Raman experiments the presence of a single-domain structure is not mandatory, but important for the determination of Raman selection rules.

Deposition at $400\,°C$ was monitored by RAS and controlled by maximizing the main surface anisotropy related RAS feature at 2 eV. After cooling to RT, LEED patterns showed a single domain (4×1) reconstruction.

The Raman measurements were performed *in situ* using a macro-Raman spectroscopy setup in near backscattering geometry. A triple Raman spectrometer with the first two stages in the subtractive configuration was used. Spectrometer entrance slits were adjusted to $100\,\mu$m for measurements shown in Figs. 1 and 3 (resolution FWHM $= 2.1$ cm^{-1}) and to $50\,\mu$m for high-resolution measurement shown in Fig. 5 (resolution FWHM $= 1.2$ cm^{-1}). The spectral resolution was

determined by the evaluation of the FWHM of incoherent emission lines from the laser plasma.

The spectrometer was equipped with an additional laser line blind in the aperture between two subtractive stages in order to reduce the contribution of the elastically scattered laser light to the spectra, in particular in the low-wave-number range. This blind was installed in the manner that both Stokes and anti-Stokes Raman spectra may be recorded simultaneously while the range ± 10 cm^{-1} to the laser line is rejected (Fig. 1). Moreover, with this setup the intensity of the elastically and inelastically scattered light can be monitored simultaneously. This makes it possible to check the local surface roughness and to verify that the suppression of the elastically scattered laser light is sufficient for measurements in the low-frequency range (down to 10 cm^{-1}).

Due to the penetration depth of light, the experimentally recorded Raman spectra are a superposition of bulk and surface phonon excitations. However, the Raman scattering cross section depends significantly on the resonance of incident and scattered light with electronic states [50]. Surface phonons couple predominantly to surface electronic states [46] as the atomic displacements related to surface phonons are confined to the few topmost atomic layers; the deformation potential scattering is mediated by surface electronic states. Similarly, bulk modes scatter predominantly via the bulk electronic states. For the Raman experiments on Si a resonance occurs at the E_1-bulk critical point of 3.4 eV [51]. Surface phonons are favorably recorded at lower energies under surface resonant conditions, using excitation laser lines close to the surface electronic transitions at 1.9 eV [52]. The Raman measurements presented in this work are performed with an excitation laser line at 1.91 eV (647.1 nm), i.e., in surface resonant conditions.

Raman spectra for different polarization configurations are essential for the verification of the symmetry of vibrational modes. The polarization sensitivity of the spectrograph, which has a strong impact on intensities of spectra taken at different polarization orientations, is an experimental obstacle in separating the information on symmetry. This problem was eliminated by using only one polarization direction inside the spectrograph and rotation of the polarization of the analyzed scattered light by Fresnel rhombs prior to the entrance into the spectrograph. By applying this technique the intensities of spectra taken at different polarization geometries are comparable.

Density-functional theory (DFT) calculations within the local density approximation [53] as implemented in the Vienna Ab initio Simulation Package (VASP) [54] were performed in order to assign the measured phonon frequencies to deformation patterns. Thereby frozen-phonon calculations [55] have been performed for both the zigzag chain geometries of the RT (4×1) phase as well as for the hexagon structure of the LT (8×2) phase. In accordance with previous phonon calculations of some of the present authors [27], an (8×4) surface unit cell with two Si bilayers modeling the substrate was used. The larger cell size minimizes numerical artifacts due to the periodic boundary conditions and gives access not only to the Γ point modes, but also to phonon modes at further high-symmetry points of the surface Brillouin (BZ) zone. Further numerical details are chosen in accordance with Ref. [27].
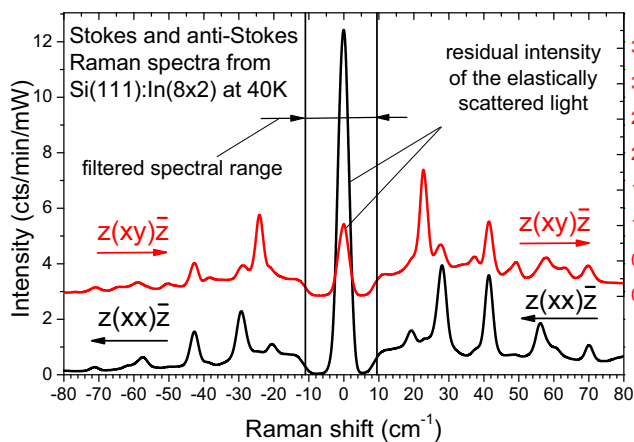

FIG. 1. Simultaneously recorded Stokes and anti-Stokes Raman spectra from In nanowires on Si(111) (8×2) reconstruction at 40 K for $z(xx)\bar{z}$ (black line) and $z(xy)\bar{z}$ (red line) polarization configurations. The spectral range filtered by the laser blind is marked. The residual intensity of elastically scattered light shows up in the center of the spectrum.

III. RESULTS AND DISCUSSION

A. Symmetry considerations

The Raman tensor determines for which polarization of incoming and scattered light a certain phonon mode is Raman "allowed" or "forbidden" [50]. The $[1\bar{1}0]$ and the $[11\bar{2}]$ crystal directions are the principal axes of light polarization for Raman backscattering on the silicon crystal (O_h point group) (111) surface.

Deformation potential scattering of the bulk TO mode is then symmetry allowed in any polarization configuration, i.e., for polarizations of incident and scattered light (E_i, E_s) along ($[1\bar{1}0],[11\bar{2}]$), along ($[1\bar{1}0],[1\bar{1}0]$), and along ($[11\bar{2}],[11\bar{2}]$), respectively [50].

Compared to bulk crystals different selection rules apply for the surface phonon modes, since the termination of the crystal reduces its symmetry. We focus on the upper layers of the structure in order to simplify the identification of the symmetries in the surface reconstruction. As shown below, low-energy vibrations involving mainly In atom displacements are strongly located in the top layer of the reconstruction. Therefore, we assume that this makes it possible to consider only the symmetries of the top layer for this class of surface vibrations.

The upper layers can be classified within the two-dimensional space groups, i.e., the so-called wallpaper groups. The atomic geometries and symmetry operation in surface elementary cells of (8×2) and (4×1) reconstructions are shown in Fig. 2. A twofold rotation, a mirror, and a glide plane can be identified in the case of the (4×1) zigzag chain structure, which classifies this structure as a "pmg" 2D space group. In the case of the (8×2) hexagon reconstruction only a glide reflection plane can be identified, thus classifying this model as a "pg" 2D space group. However, none of the 2D symmetry operations are in conflict with the symmetry of the Si substrate. Hence, they can be transferred to the three-dimensional symmetry operations. The associated 3D space groups are the orthorhombic C_{2v} and the monoclinic C_S for the (4×1) and (8×2) reconstructions, respectively. The corresponding Raman tensors are listed in Ref. [50].

With respect to the Si crystal, the main axes (x,y,z) correspond to ($[11\bar{2}]$, $[1\bar{1}0]$, $[111]$). Due to incident and analyzed E-field vector orientation parallel to the surface, the Raman tensor can be reduced to the two dimensions x and y and thus is given as

$$\mathbf{R}(A') = \begin{pmatrix} a & 0 \\ 0 & b \end{pmatrix}; \qquad \mathbf{R}(A'') = \begin{pmatrix} 0 & c \\ c & 0 \end{pmatrix}. \qquad (1)$$

The corresponding normal modes separate into A' and A'' surface modes which are symmetry allowed under parallel or perpendicular polarization configurations, respectively [44].

The Raman spectra in Fig. 3 are taken under four different polarization geometries: A' modes appear under the (x,x) and (y,y) configurations with components a and b, and A'' modes under the (y,x) or (x,y) configurations with tensor component c, respectively. The associated atomic displacement patterns are either transformation invariant with respect to the respective symmetry operation (in the case of A') or not transformation invariant (in the case of A''). The difference in the two A' scattering configurations (components a, b) results
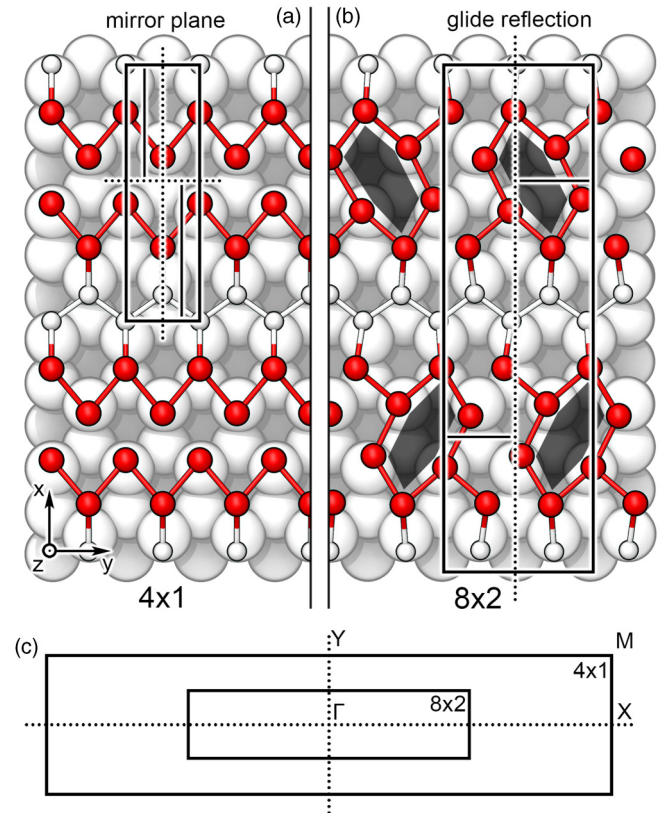

FIG. 2. Surface cells and symmetry elements in the room-temperature (4×1) (a) and low-temperature In:Si(111)(8×2) phase (b), respectively. The surface coordinate system is indicated ($x \| [11\bar{2}]$, $y \| [1\bar{1}0]$, $z \| [111]$ in the Si bulk high-symmetry directions). In (c) the corresponding surface Brillouin zones with characteristic points are shown.

from the fact that the surface unit cell is highly anisotropic, with the In chains extending along the $[1\bar{1}0]$ direction. This has a strong impact on the surface electronic band structure and related surface optical transitions which are important for the Raman scattering process.

B. Surface phonons

Surface phonon modes in the range from 20 up to 500 cm^{-1} have been determined by surface Raman spectroscopy for (4×1) and (8×2) and have been reported in Ref. [40]. The surface vibrational modes at high frequencies involve mainly displacements of the Si atoms in the subsurface layers underneath the In-adsorbate layer. In the low-frequency range ($\lesssim 100$ cm^{-1}) the surface vibrational modes involve mainly displacements of the In atoms of the upper atomic layer. The separation in these frequency domains is due to the large atomic mass difference of In (115 amu) and Si (28 amu). The phase transition induces structural changes mainly in the uppermost layer. Thus, a detailed analysis of the vibrational modes in the lower-frequency range should provide the essential information on the structure of the low- and room-temperature phases. For this purpose we have recorded high-resolution Raman spectra (spectral resolution of 1.2 cm^{-1}) in the low-frequency range down to 10 cm^{-1}.
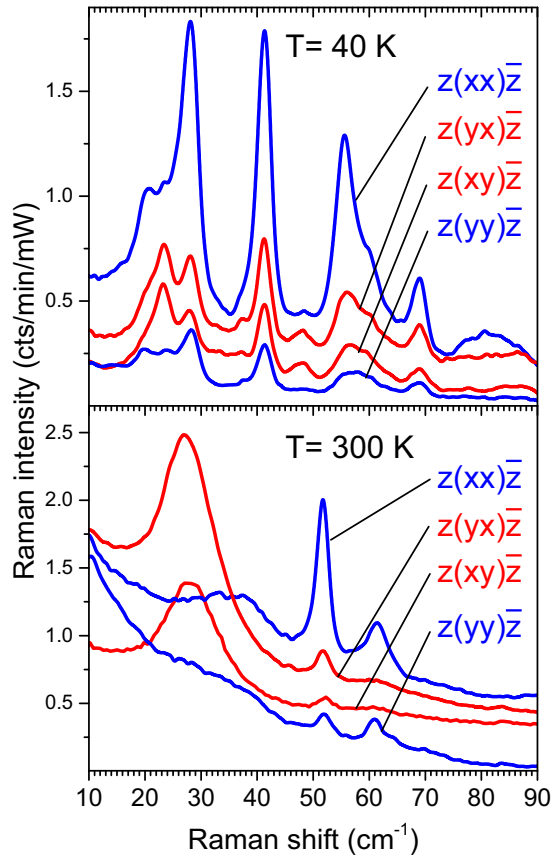
FIG. 4. Deconvolution of contributions to the Raman spectra of the (4×1) phase at room temperature in $z(xx)\bar{z}$ and $z(yx)\bar{z}$ scattering geometries shown in Fig. 3. Measurements were fitted with Voigt line-shape peaks. Extracted frequencies and linewidths are shown in Table I together with the Raman symmetry.

FIG. 3. Polarized Raman scattering from low-temperature (8×2) (solid blue lines) and room-temperature (4×1) (dotted red lines) phases. Spectra taken at $z(xx)\bar{z}$, $z(xy)\bar{z}$, $z(yy)\bar{z}$, $z(yx)\bar{z}$ scattering geometries are shown. The polarization vector of the exciting laser radiation is perpendicular and parallel to the direction of the indium chains (y).

In Fig. 3 Raman spectra from the RT (4×1) and LT (8×2) phases are shown. Four different polarization geometries are taken for both reconstructions in order to check the mode symmetry by Raman selection rules. The spectra at low and room temperatures show strong differences. In the RT (4×1) case the spectral line shape is similar to the previously published spectra [40]. In A' geometry one strong mode at 51.7 cm^{-1} and weak modes at 31.2, 38.1, and 61.4 cm^{-1} are seen, while in the A'' geometry one strong mode at 27.5 and weak modes at 17.9 and 51.7 cm^{-1} appear. It is worth noting that only two polarization geometries were investigated in Ref. [40] and, moreover, the weak A'' mode appearing as a shoulder at 17.9 cm^{-1} could not be identified at all. This was possible by the reduced stray light in the measurement. While in Ref. [40] an intensive, elastically scattered background was assumed, in the present work the influence of the elastically scattered light can be measured as described above. Hence, a broad inelastically scattered background is found in the new set of measurements, represented in the fits in Fig. 4 as Lorentzian line shapes centered at zero frequency shift. The background is induced by electronic Raman scattering on collective electron excitations.

The two A' measurements show significant differences of Raman efficiency for polarized light oriented along and perpendicular to In nanowires, in particular for the mode at
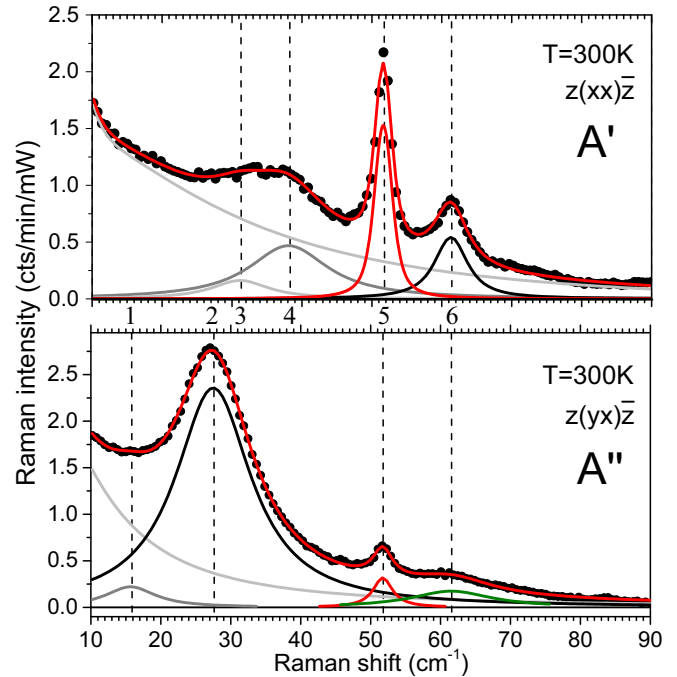
51.7 cm^{-1}. On the other hand, the two A'' geometries do not show significant differences. This is expected due to the a, b, and c components of the A' and A'' Raman tensors, respectively.

Much more structured Raman spectra are observed for the (8×2) phase. In the A' case prominent vibrational modes at 19.6, 28.3, 41.4, 48.1, 55.5, 60, and 69 cm^{-1} arise; in the A'' case prominent modes are found at 23.4, 41.4, 48.1, 63.5, and 69 cm^{-1}. The Raman spectra for the two A'' configurations are very similar, while pronounced differences in Raman intensity and partly also in spectral line shape occur in the two A' geometries. As stated above for (4×1), this is a consequence of the strongly anisotropic structure of the two phases and reflected by the Raman tensors components $a \neq b$ in Eq. (1), according to the monoclinic C_S symmetry.

The pure inspection of eigenfrequencies of the surface modes at low and room temperatures might suggest that the (4×1) modes could be just broadened and frequency-shifted (8×2) signatures, and clear identification of distinct spectral fingerprints of the two phases might be difficult. However, there are clear indications that we are indeed dealing with distinct structural phases and a first-order transition.

Apart from eigenfrequencies we also determine symmetries of the eigenmodes from Raman selection rules. Both eigenfrequencies and symmetries are unique mode properties and used to identify eigenmodes. By taking symmetries of RT and LT spectra into account (see Fig. 3) it is evident that the strong low-frequency A' modes have no counterpart in the RT spectra under A' symmetry. Thus, distinct fingerprints for the LT and RT phase indeed exist, which point towards a first-order

transition between two distinct structural phases (according to distinct local minima in the total energy).

In the case of an order-disorder transition, the Raman spectra would behave distinctly different: The (8×2) phase would be the ordered ground-state structure and with Raman we would see the surface phonon modes at the Brillouin zone center at LT. On warming up, disorder in the surface structure would arise from domain flipping. This leads to a disorder activated Raman scattering of phonon modes outside the Brillouin zone center, according to the phonon density of states
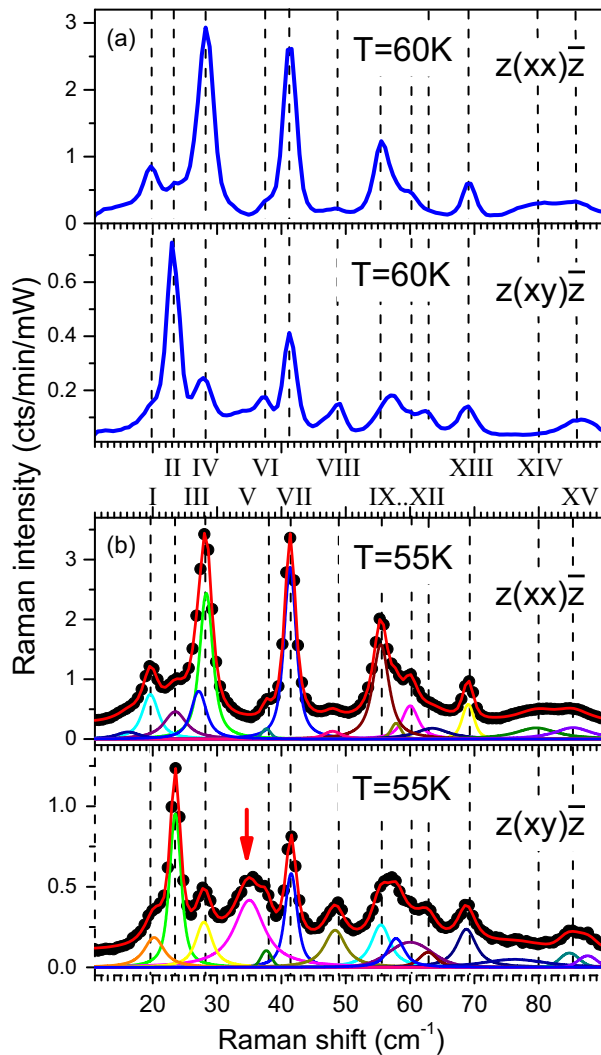

FIG. 5. Comparison of high-resolution Raman spectra at 55 K [black dots in (b)] in $z(xx)\bar{z}$ and $z(xy)\bar{z}$ scattering geometries with spectra from a different sample at 60 K (a) (blue lines in the top panels). For better comparability, backgrounds are subtracted in all spectra shown in order to outline the phonon contribution to the scattered intensity. Both sets of spectra were fitted with Voigt line-shape peaks with coupled frequencies of the peaks dominant in $z(xx)\bar{z}$ or in $z(xy)\bar{z}$ scattering geometry. The same surface phonon modes can be derived from the fits in both cases. In the case of sample (b) some feature of supercooled (4×1) regions on the surface appear in addition to the (8×2) modes (marked with a red arrow). In the case of sample (a) no such feature shows up, indicating that the surface homogeneity depends on individual sample conditions (preparation, storage time in UHV).

TABLE I. Measured (4×1) RT phonon mode frequencies (cm^{-1}) and assigned calculated modes in the range from 10 to 90 cm^{-1}. The values are extracted from measurements by fitting the spectra with Voigt line-shape peaks. The Gaussian component corresponds to the spectral resolution of 1.2 cm^{-1}. The values are extracted from fits of spectra shown in Fig. 3 taken at room temperature. Measured values are compared with calculated frequencies at $(4 \times 1)_\Gamma$, with vibrational patterns shown in Fig. 6 (indicated by letters). The errors are given for the 90% confidence interval.

No.	Energy	Linewidth	Symmetry	Theory $(4 \times 1)_\Gamma$
1	17.9 ± 1.8	12.6 ± 5.0	A''	20.2 (a)
2	27.5 ± 0.1	6.6 ± 0.1	A''	32.3 (c)
3	31.2 ± 2.5	9.2 ± 7.8	A'	44.4 (d)
4	38.1 ± 0.5	12.8 ± 3.4	A'	50.8 (e)
5	51.7 ± 0.1	1.8 ± 0.2	A', A''	64.6 (j)
6	61.4 ± 0.1	4.5 ± 0.2	A', A''	78.9 (l)

in the entire Brillouin zone. In Raman we would find additional modes showing up besides the modes seen at LT. The according behavior has been found, for instance, by Raman spectroscopy on Ge(001) surfaces at RT and LT, i.e., for the $c(4 \times 2)$ and the disorder-induced $p(2 \times 1)$ surface structure [47].

The main difference between the present measurements for the (4×1) and (8×2) reconstructions at RT and LT, respectively, and earlier data [40] is an improvement of the spectral resolution from about 5 to 1.2 cm^{-1} for the (8×2) phase (in Fig. 5). This is essential for the deconvolution of the Raman spectra into the individual surface modes, in particular for the (8×2) LT structure.

For the verification of the structure by its vibrational properties we compare the eigenfrequencies and symmetry properties of the measured and calculated vibrational modes. For the latter reason the analysis of vibrational patterns is important. A comparison of experimental results and theoretical calculations is shown in Tables I and II for the (4×1) and

TABLE II. Measured (8×2) LT phonon mode frequencies (cm^{-1}) and assigned calculated modes in the range from 10 to 90 cm^{-1}, extracted from fits in Fig. 5. The errors are given for the 90% confidence interval.

No.	Expt. (cm^{-1})	FWHM	Symm.	Theory (8×2)
I	19.6 ± 0.1	4.0 ± 0.6	A'	20.0 [Table III(b), $8 \times 2_{\Gamma,\Gamma}$]
II	23.4 ± 0.1	2.4 ± 0.2	A''	22.2 [Table III(c), $8 \times 2_{\Gamma,\Gamma}$]
III	27.1 ± 0.5	3.7 ± 1.3	A'	26.8 [Table IV(a), $8 \times 2_{\Gamma,M}$]
IV	28.3 ± 0.1	2.9 ± 0.4	A'	27.4 [Table IV(a), $8 \times 2_{\Gamma,X}$]
V$_{4 \times 1}$	35.0 ± 0.4	9.5 ± 3.6	A''	32.3 [Table III(c), $4 \times 1_\Gamma$]
VI	37.7 ± 0.1	1.0 ± 0.5	A'	
VII	41.4 ± 0.1	2.5 ± 0.1	A', A''	53.8 [Table IV(d), $8 \times 2_{\Gamma,X}$]
VIII	48.1 ± 0.2	2.8 ± 0.8	A', A''	59.0 [Table III(l), $8 \times 2_{\Gamma,Y}$]
IX	55.5 ± 0.0	4.0 ± 0.2	A'	69.6 [Table III(j), $8 \times 2_{\Gamma,\Gamma}$]
X	57.8 ± 0.1	1.4 ± 1.0	A'	
XI	60.0 ± 0.1	4.1 ± 1.1	A'	
XII	63.5 ± 0.5	10.4 ± 5.0	A', A''	
XIII	69.0 ± 0.0	1.4 ± 0.2	A'	87.2 [Table III(l), $8 \times 2_{\Gamma,\Gamma}$]
XIV	80.6 ± 0.3	11.4 ± 6.0	A'	
XV	85.4 ± 0.3	6.7 ± 0.7	A', A''	

(8×2) reconstructions, respectively. A detailed discussion of the mode assignment is presented in the following.

C. Vibrational mode assignment for the (4×1) phase

The comparison of measured and calculated frequencies and symmetries of the surface vibrations confirms the structural model of the (4×1) phase and underlines the accuracy of the present DFT approach for surface vibrations. In the case of the RT (4×1) phase a systematic downshift in frequency of the calculated modes with regard to experiment is expected, since calculations do not correct for finite-temperature effects. The temperature effect becomes evident in the case of the supercooled (4×1) domains which show a Raman mode at approximately 35 cm^{-1} (see Fig. 7). Additional temperature-dependent Raman spectra (not shown here) show that at RT this mode refers to the A'' mode at 27.5 cm^{-1}, i.e., 8 cm^{-1} lower than at 55 K.

The Raman spectra for the (4×1) phase shown in Fig. 3 show several A' and A'' modes in the spectral range up to 90 cm^{-1} which can be assigned to distinct surface vibrational patterns similar to previous work by Fleischer *et al.* [40]. Already judging from the Raman spectra alone, it is evident that these modes are surface vibrational modes, since they are uniquely related to the In nanowire structure formation. This can be seen from the comparison with the Raman spectra of the clean Si(111) surface [48]. By comparison to the frozen-phonon calculations a full microscopic picture of the related modes and their displacement patterns is possible. In Table I an assignment of the calculations together with the experimental information on eigenfrequency and Raman selection rules is given. The calculated displacement patterns of the Γ point modes of the RT (4×1) phase are shown in Fig. 6, with the according A' and A'' symmetry classification and phonon frequencies compiled in Table III.

D. Vibrational mode assignment for the (8×2) phase

The assignment of (8×2) is more cumbersome due to a larger surface elementary cell and the more complex surface structure. In Fig. 5(b) a set of Raman spectra at low temperature is shown for A' and A'' polarization configurations, for a spectral resolution of 1.2 cm^{-1}. For comparison another set of Raman spectra taken at 60 K is given in Fig. 5(a). We would like to note that Raman spectra in Figs. 3, 5(a), and 5(b) refer to three different samples. All (8×2) modes, present in low-temperature measurements in Fig. 3 and discussed above, are found again. Nevertheless, the improved spectral resolution is essential for the decomposition of the spectra into individual phonon lines for the following discussion of the eigenmodes.

The A'' mode at ca. 35 cm^{-1} related to the undercooled (4×1) domains corresponds to the shear mode (upshifted from ca. 28 cm^{-1} at RT to ca. 35 cm^{-1} at LT) shown in Fig. 6(c). The assignment of this mode is proven by a detailed analysis of its temperature dependence (not shown here). This analysis clearly shows the coexistence of the (4×1) and (8×2) phases on the surface below the phase transition temperature of 125 K, a result which we find regularly during different sets of experiments, however with distinct relative mode intensities. Consequently, (4×1) and (8×2) domains coexist
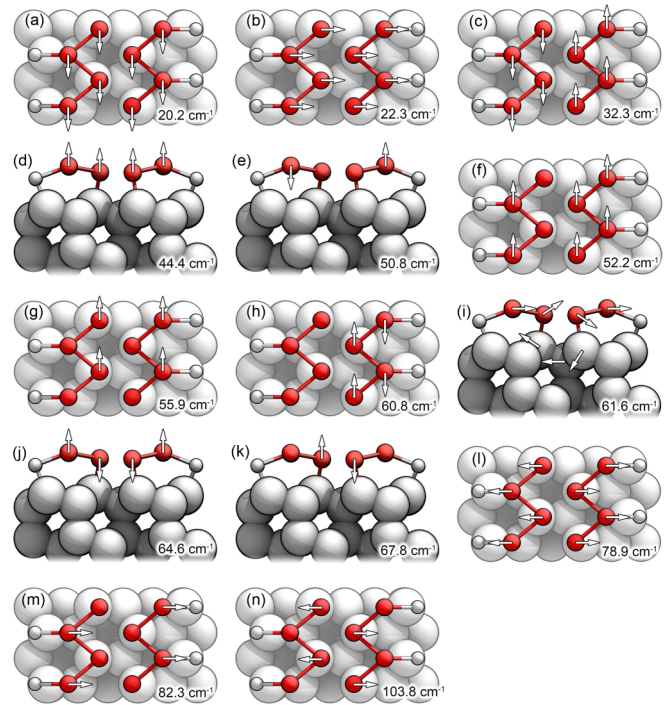

FIG. 6. Calculated displacement vectors of surface-localized phonon modes of the (4×1) phase at the Γ point of the surface Brillouin zone [see also Table III, (4×1)$_\Gamma$].

on the surface, with distinct domain occupation. As shown previously, the RT phase can be stabilized at temperatures below the phase transition by adsorbates [36,56]. Moreover, the doping concentration of the Si substrate may influence the phase transition due to related differences in the surface charge [38]. In this case the undercooled (4×1) phase domains may

TABLE III. Calculated frequencies (in cm^{-1}) of surface-localized phonon modes of the (4×1) phase at the Γ and the Y point of the surface Brillouin zone. The notation corresponds to Fig. 6. Also shown are the calculated frequencies of those surface-localized phonon modes of the (8×2) phase that correspond largely to the symmetric (Γ)/antisymmetric (Y) combinations of the (4×1) modes that arise from the doubling of the unit cell size perpendicular to the chain direction.

| Mode	Symm.	$4 \times 1_\Gamma$	$4 \times 1_Y$	$8 \times 2_{\Gamma,\Gamma}$	$8 \times 2_{\Gamma,Y}$
(a) x disp.	A''	20.2	24.8	19.2	23.5
(b) y disp.	A'	22.3	44.2	20.0	46.3
(c) Shear	A''	32.3	25.3	22.2	18.3
(d) z disp.	A'	44.4	45.2	46.9	47.8
(e) z rocking	A'	50.8	51.5	53.0	52.7
(f) Outer disp.	A''	52.2	70.7	51.0	67.7
(g) Inner/outer	A''	55.9	56.7	81.6	71.3
(h) Single chain	A''	60.8	62.8	72.3	75.4
(i) Ads./subst.	A'	61.6	118.7	57.9	117.7
(j) Butterfly	A'	64.6	64.3	69.6	69.2
(k) Inner	A'	67.8	67.6	68.8	67.4
(l) Lateral disp.	A'	78.9	51.9	87.2	59.0
(m) Outer lat.	A'	82.3	93.2	105.7	102.0
(n) Inner lat.	A'	103.8	105.1	114.3	129.1
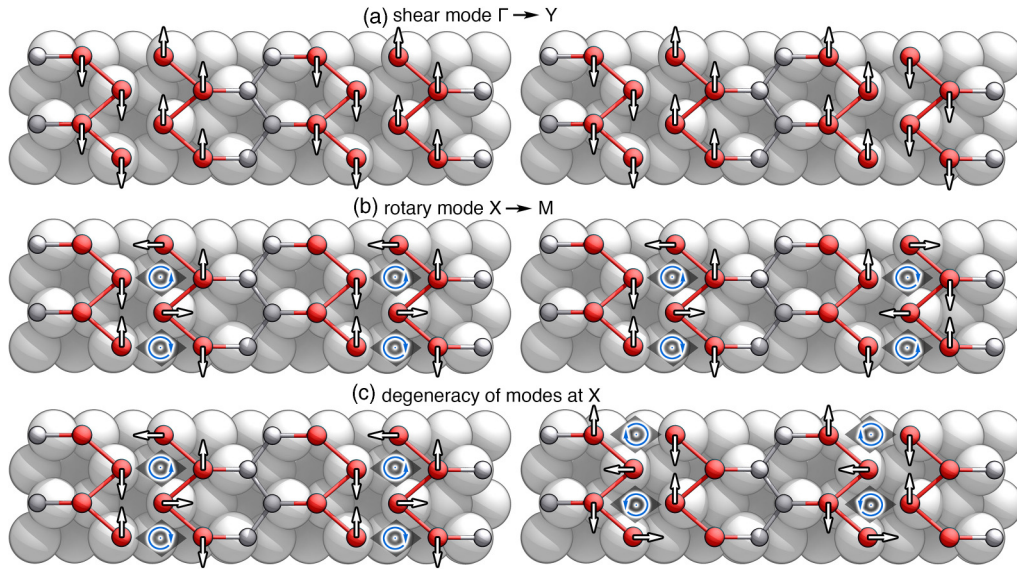
FIG. 7. Phonon modes at the $\Gamma \leftrightarrow Y$ and $X \leftrightarrow M$ points of the surface Brillouin zone (SBZ) are symmetry related by an inversion of the corresponding eigenvectors on the neighboring chains, illustrated at the examples of the (a) shear and (b) rotary modes, indicating rather weak interchain interactions. Due to the much stronger intrachain interactions, the X modes in contrast cannot be obtained by simple inversion of the Γ eigenvectors in the next unit cell along the wire direction. Note that SBZ edge modes of the (4×1) unit cell, such as X, Y, and M modes, are folded back to the Γ point within the (8×2) unit cell, enabling Raman scattering at those modes in the low-temperature phase. (c) Near-degeneracy of the X point modes with respect to a 180° rotation of the eigenvector around the surface normal. Both modes shown are genuinely different, because the rotational symmetry is broken by the underlying substrate.

be induced by a small contamination from the residual gas due to storage (8 h at 1×10^{-10} mbar) in UHV. Both sets of experiments were performed on Si substrates of different bulk doping concentration, i.e., with medium and high n type for the first set and second set, respectively ($n < 10^{14}$/cm^3, $n > 10^{18}$/cm^3).

The dominant features in the high-resolution Raman spectra marked by the dashed lines in Fig. 5 are the characteristic surface phonon modes of the (8×2) structure. By fitting the Raman spectra with a set of Voigt functions we obtain eigenfrequencies, widths and amplitudes of these surface mode related Raman lines. For the data fitting the same mode eigenfrequencies are used in both polarization configurations, as indicated by the thin vertical lines. In total, 15 oscillators are

used to describe the surface phonon spectrum of the (8×2) phase. In Table II a compilation of the fitting parameters is given for these modes. Assignments are always made such that Raman selection rules and symmetry of the displacement patterns, calculated by DFT, agree.

Upon the (4×1) to (8×2) phase transition two mechanisms are expected to induce modifications in the Raman spectra: (i) One enables Raman scattering at edge modes of the (4×1) surface Brillouin zone (SBZ) due to backfolding to the Γ point (cf. Fig. 7), and (ii) the other is a change of the phonon frequencies due to atomic structure modifications within the respective unit cell (compare Fig. 8 and 9).

Since only small structural changes occur upon the phase transition from (4×1) to (8×2), as seen in the corresponding
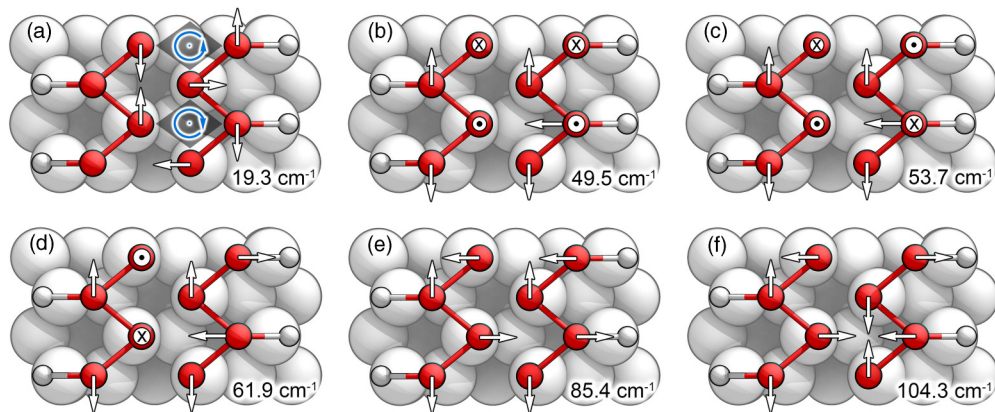

FIG. 8. Calculated displacement vectors of surface-localized phonon modes of the (4×1) phase at the X point of the surface Brillouin zone. Each mode is nearly degenerate with a displacement pattern [not shown, but illustrated conceptually in Fig. 7(c)] that is rotated by 180° with respect to the mode shown here.
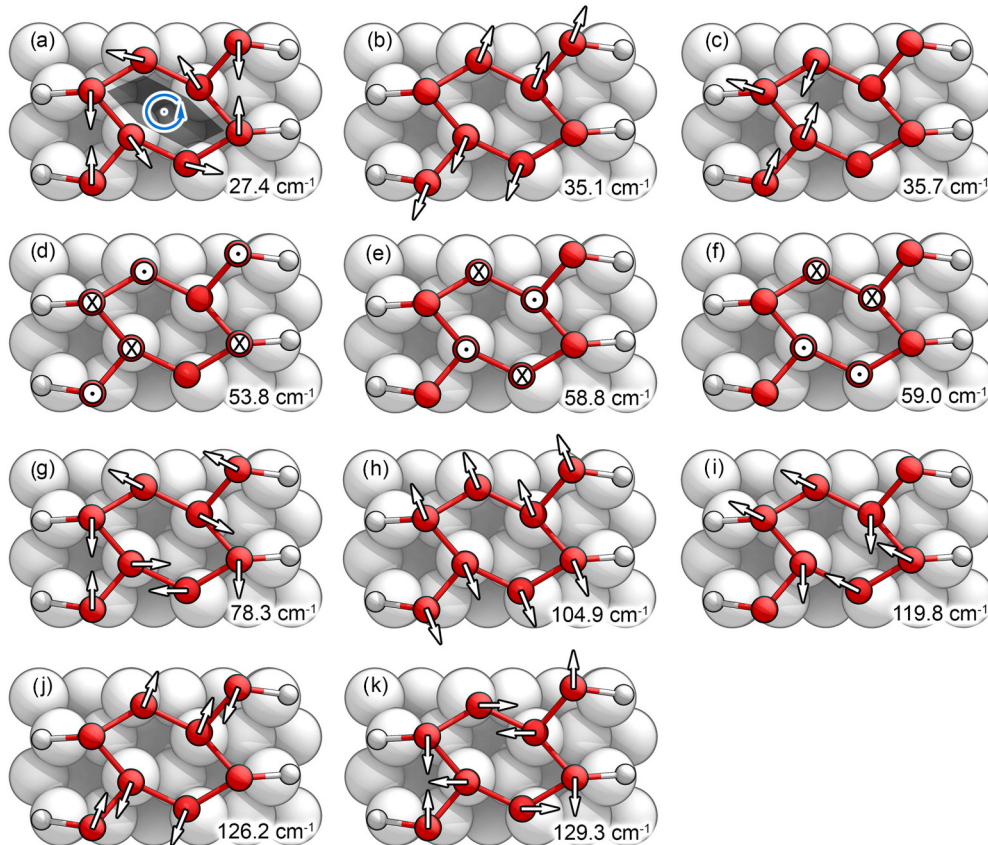
FIG. 9. Calculated displacement vectors of surface-localized phonon modes of the (8×2) phase at the Γ point of the surface Brillouin zone. Only the modes are shown that are not trivially obtained by symmetric/antisymmetric combinations of (4×1) phase modes due to the unit cell doubling perpendicular to the chain direction, i.e., modes that correspond widely to Γ and M point modes of the (4×1) phase. The modes shown here correspond formally to X point modes of the (4×1) phase, but deviate significantly, as seen by comparison to Fig. 8.

reconstruction models, the eigenfrequencies of the (4×1) $\overline{\Gamma}$-point modes are expected to be largely similar in the two phases. As listed in Table III, most of the (4×1) $\overline{\Gamma}$ modes feature a counterpart in the (8×2) phase with nearly identical eigenvectors and calculated eigenfrequencies agreeing within a few cm^{-1}. Notable exceptions are the modes (c), (g), (h), (l), (m), and (n), which involve significant stretching of the surface In-In bonds that are modified upon (8×2) hexagon formation. These modes still show similar eigenvectors in both phases but different frequencies with deviations of up to 25 cm^{-1}.

Moreover, the doubling of the surface elementary cell in the (8×2) reconstruction in both directions, along and perpendicular to In chains, results in an increase of the number of modes, simply due to quadruplication of the atoms in the corresponding elementary cell. Thus, SBZ edge modes of the (4×1) unit cell are folded back to the SBZ center of the (8×2) unit cell, allowing for Raman scattering at (4×1)-like phonons at $\overline{X}$, $\overline{M}$, and $\overline{Y}$ points in the SBZ.

Due to the comparatively weak interchain interaction in the (8×2) phase, the doubling of the surface unit cell perpendicular to the chain direction induces symmetric and antisymmetric modes, which formally correspond to $\overline{\Gamma}$ and $\overline{Y}$ point modes of the (4×1) unit cell, but are $\overline{\Gamma}$ point modes of the (8×2) unit cell due to backfolding [see Fig. 7(a)]. As discussed above, many of the calculated phonon frequencies agree within a few cm^{-1}, confirming the backfolding mechanism. On the other

hand, large deviations of up to 25 cm^{-1} arise for some other modes, related to the structure modification within the unit cell. This differs according to the individual mode displacement patterns, respectively.

In contrast, the intrachain interactions are much stronger as compared to interchain interactions. The resulting phonon dispersion along the $\overline{\Gamma}$-$\overline{X}$ direction leads to modes that are very different in character at the $\overline{X}$ point as compared to $\overline{\Gamma}$ point. We find the $\overline{X}$ point modes to be rather sensitive to structural details of the In induced structure, since these modes predominantly involve movements of the In-In bonds that are modified upon hexagon formation. During the $(4 \times 1) \rightarrow (8 \times 2)$ phase transition, the eigenvectors and eigenfrequencies of the $\overline{X}$ modes undergo characteristic changes. The corresponding calculations for the (8×2) mode eigenvectors and eigenfrequencies are shown in Fig. 9 and Table IV, respectively. Again, due to the weak interchain interaction we observe very similar symmetric and antisymmetric modes corresponding formally to $\overline{X}$ and $\overline{M}$ point modes of the (4×1) SBZ (see Fig. 7), analogous to the $\overline{\Gamma}$-$\overline{Y}$ modes discussed above.

E. Discussion of the mode assignment

It is found that for most calculated frequencies, in particular of the (4×1) structure, a slight systematic overestimation is observed compared to the Raman measurements, most

TABLE IV. Calculated frequencies (in cm^{-1}) of surface-localized phonon modes of the (8×2) phase at the $\overline{\Gamma}$ point of the surface Brillouin zone that correspond widely to the antisymmetric combinations of the (4×1) modes that arise from the doubling of the unit cell size along ($\overline{X}$) and along ($\overline{M}$), respectively. The notation corresponds to Fig. 9. Calculated frequencies (in cm^{-1}) of the related surface-localized phonon modes of the (4×1) phase at the $\overline{X}$ and the $\overline{M}$ points of the surface Brillouin zone are given, respectively. The notation of the $\overline{X}$ modes corresponds to Fig. 8.

Mode	$(8 \times 2)_{\overline{\Gamma}, \overline{X}}$	$(8 \times 2)_{\overline{\Gamma}, \overline{M}}$	Mode	$(4 \times 1)_{\overline{X}}$	$(4 \times 1)_{\overline{M}}$
(a)	27.4	26.8	(a)	15.3, 19.3	19.6, 22.3
(b)	35.1	35.0			
(c)	35.7	35.2			
(d)	53.8, 54.5	54.9, 53.6	(b)	49.5, 49.6	49.2, 49.7
(e)	58.8	59.6	(c)	53.3, 53.7	52.8, 53.1
(f)	59.0	57.0	(d)	61.0, 61.9	58.5, 59.9
(g)	78.3	77.1	(e)	84.7, 85.4	87.0, 88.1
(h)	104.8	104.9	(f)	104.3, 104.4	102.8, 104.4
(i)	119.8	122.4			
(j)	126.2	126.4			
(k)	129.3	128.5			

likely due to anharmonic effects present at room temperature. The systematic overbinding inherent to the local-density approximation (LDA) may also contribute. In particular for the low-temperature (8×2) structure, where anharmonicities are absent, the calculated frequencies fit excellently to the Raman modes within a small error in frequency of a few cm^{-1}.

Based on these calculations a full microscopic picture of the dominating surface Raman modes in terms of In-Si surface vibrational eigenmodes and their relation between (4×1) and (8×2) phases has been achieved. The surface vibrational modes correspond to the various surface optical phonon branches at the $\overline{\Gamma}$ point of the surface Brillouin zone. As there are a large number of vibrational modes detected with high spectral precision, a comparison with according frozen-phonon calculation is a versatile check of the surface structure. The calculation shows that, in fact, the In hexagon structure is the correct structure model of the (8×2) phase.

Nevertheless, the determination of mode symmetries and eigenfrequencies is not straightforward. First of all, symmetry selection rules depend on structural perfection of the surface which is limited by surface steps, surface defects, and residual gas adsorbates. Second, the surface has an anisotropic low-symmetry structure and the unit cell contains a large number of atoms with respect to the missing periodicity perpendicular to the surface. Thus, many surface modes may exist and there is no strict limit for the number of surface phonon modes. In practice, the number of surface modes is limited due to the degree of surface localization of the respective mode displacement patterns. Experimentally, due to the surface localization, respective phonon modes show surface electronic resonances distinct from the bulk resonance which make them well observable on the signal background of bulk phonon mode scattering [49].

Within the present work we have treated low-frequency In-Si vibrational modes that are localized to the upper few atomic planes. The degree of surface localization can be

verified from the DFT calculations, which enables us to identify clear-cut surface modes. Nevertheless, the assignment of experimental Raman lines may remain difficult since in a low-symmetry structure the resonant Raman cross section may vary significantly for the different modes, depending on the deformation potential modulation of the surface electronic states. Thus, strong differences in Raman scattering efficiency between distinct surface vibrational modes may occur which superimpose the symmetry selection rules. Therefore, specific surface modes appear weak in Raman intensity, while others have a large intensity. This is, in fact, observed in the present case and the analysis of the surface vibrational spectrum by DFT calculations is very helpful to achieve a clear mode assignment.

In the hexagon model of the (8×2) phase the doubling of the elementary surface cell in the chain direction results from noticeable structural changes along the chains, while the doubling in the perpendicular direction is related to a weak correlation between neighboring chain structures. The effect of backfolding and the correlations of zone edge modes in (4×1) with zone center modes in (8×2) has been revealed in detail. The agreement between vibrational modes calculated for room-temperature and low-temperature zigzag chain models and hexagonal models with measured phonon frequencies for both phases confirms the structural models and the first-order phase transition.

The assignments of the calculated and measured frequencies are also supported by the temperature-dependent frequency shifts which are not presented here as they go beyond the scope of the paper and consequently are to be published elsewhere.

We would like to note that the eigenfrequencies calculated for the trimer model of the (8×2) phase [28] differ significantly from the experimental results shown here.

IV. SUMMARY

In conclusion, we used Raman spectroscopy in conjunction with frozen-phonon calculations within the density-functional theory to explore the vibrational properties on the In:Si(111) surface. Both the low-temperature (8×2) and the room-temperature (4×1) phases are characterized by their own distinct sets of phonon modes. This rules out the order-disorder scenario for the metal-insulator transition of the In nanowire array. Changes in the Raman spectra related to the phase transition from the (4×1) to (8×2) phase are caused by two effects: (i) structural changes of the surface reconstruction, and (ii) backfolding of edge modes of the (4×1) surface Brillouin zone into the Γ point of the (8×2) SBZ. In particular, we find the $\overline{\Gamma}$ modes to be largely preserved upon the $(4 \times 1) \longrightarrow (8 \times 2)$ phase transition, while the $\overline{X}$ point modes undergo stronger modifications of their eigenvectors and eigenfrequencies. Each $\overline{\Gamma}$ and $\overline{X}$ mode is accompanied by an antisymmetric mode, corresponding formally to $\overline{Y}$ and $\overline{M}$ modes of the (4×1) SBZ, respectively. This infers a strong/weak phonon dispersion along/perpendicular to the In wire direction, caused by strong intrachain and weak interchain interactions. The excellent agreement between the measured phonon modes and the calculations in particular for the (8×2)

low-temperature phase of the In:Si(111) surface confirms clearly the hexagon model.

[1] F. J. Himpsel, K. N. Altman, R. Bennewitz, J. N. Crain, A. Kirakosian, J. L. Lin, and J. L. McChesney, One-dimensional electronic states at surfaces, J. Phys.: Condens. Matter **13**, 11097 (2001).

[2] C. Blumenstein, J. Schäfer, S. Mietke, S. Meyer, A. Dollinger, M. Lochner, X. Y. Cui, L. Patthey, R. Matzdorf, and R. Claessen, Atomically controlled quantum chains hosting a Tomonaga-Luttinger liquid, Nat. Phys. **7**, 776 (2011).

[3] J. Aulbach, J. Schäfer, S. C. Erwin, S. Meyer, C. Loho, J. Settelein, and R. Claessen, Evidence for Long-Range Spin Order Instead of a Peierls Transition in Si(553)-Au Chains, Phys. Rev. Lett. **111**, 137203 (2013).

[4] P. C. Snijders and H. H. Weitering, Colloquium: Electronic instabilities in self-assembled atom wires, Rev. Mod. Phys. **82**, 307 (2010).

[5] W. G. Schmidt, S. Wippermann, S. Sanna, M. Babilon, N. J. Vollmers, and U. Gerstmann, In-Si(111)(4×1)/(8×2) nanowires: Electron transport, entropy, and metal-insulator transition, Phys. Status Solidi B **249**, 343 (2012).

[6] O. Bunk, G. Falkenberg, J. H. Zeysing, L. Lottermoser, R. L. Johnson, M. Nielsen, F. Berg-Rasmussen, J. Baker, and R. Feidenhans'l, Structure determination of the indium-induced Si(111)-(4×1) reconstruction by surface x-ray diffraction, Phys. Rev. B **59**, 12228 (1999).

[7] J.-H. Cho, D.-H. Oh, K. S. Kim, and L. Kleinman, Weakly rorrelated one-dimensional indium chains on Si(111), Phys. Rev. B **64**, 235302 (2001).

[8] J. Nakamura, S. Watanabe, and M. Aono, Anisotropic electronic structure of the Si(111)-(4×1) In surface, Phys. Rev. B **63**, 193307 (2001).

[9] R. H. Miwa and G. P. Srivastava, Atomic geometry, electronic structure and image state for the Si(111)-In(4×1) nanowire, Surf. Sci. **473**, 123 (2001).

[10] S. Wang, W. Lu, W. G. Schmidt, and J. Bernholc, Nanowire-induced optical anisotropy of the Si(111)-In surface, Phys. Rev. B **68**, 035329 (2003).

[11] K. Fleischer, S. Chandola, N. Esser, W. Richter, and J. F. McGilp, Phonon and polarized reflectance spectra from Si(111)-(4×1)In: Evidence for a charge-density-wave driven phase transition, Phys. Rev. B **67**, 235318 (2003).

[12] J.-H. Cho, J.-Y. Lee, and L. Kleinman, Electronic structure of one-dimensional indium chains on Si(111), Phys. Rev. B **71**, 081310(R) (2005).

[13] S.-F. Tsay, Atomic and electronic structure of the (4×1) and (8×2) In/Si(111) surfaces, Phys. Rev. B **71**, 035207 (2005).

[14] X. Lopez-Lozano, A. Krivosheeva, A. A. Stekolnikov, L. Meza-Montes, C. Noguez, J. Furthmüller, and F. Bechstedt, Reconstruction of quasi-one-dimensional In/Si(111) systems: Charge- and spin-density waves versus bonding, Phys. Rev. B **73**, 035430 (2006).

[15] H. W. Yeom, S. Takeda, E. Rotenberg, I. Matsuda, K. Horikoshi, J. Schaefer, C. M. Lee, S. D. Kevan, T. Ohta, T. Nagao, and S. Hasegawa, Instability and Charge Density Wave of Metallic Quantum Chains on a Silicon Surface, Phys. Rev. Lett. **82**, 4898 (1999).

[16] T. Tanikawa, I. Matsuda, T. Kanagawa, and S. Hasegawa, Surface-State Electrical Conductivity at a Metal-Insulator Transition On Silicon, Phys. Rev. Lett. **93**, 016801 (2004).

[17] J. R. Ahn, J. H. Byun, H. Koh, E. Rotenberg, S. D. Kevan, and H. W. Yeom, Mechanism of Gap Opening in a Triple-Band Peierls System: In Atomic Wires on Si, Phys. Rev. Lett. **93**, 106401 (2004).

[18] S. J. Park, H. W. Yeom, S. H. Min, D. H. Park, and I. W. Lyo, Direct Evidence of the Charge Ordered Phase Transition of Indium Nanowires on Si(111), Phys. Rev. Lett. **93**, 106402 (2004).

[19] J. Guo, G. Lee, and E. W. Plummer, Intertwined Electronic and Structural Phase Transitions in the In/Si(111) Interface, Phys. Rev. Lett. **95**, 046102 (2005).

[20] S. J. Park, H. W. Yeom, J. R. Ahn, and I. W. Lyo, Atomic-Scale Phase Coexistence and Fluctuation at the Quasi-One-Dimensional Metal-Insulator Transition, Phys. Rev. Lett. **95**, 126102 (2005).

[21] C. Gonzalez, J. Ortega, and F. Flores, Metal-insulator transition in one-dimensional in-chains on Si(111): Combination of a soft shear distortion and a double-band peierls instability, New J. Phys. **7**, 100 (2005).

[22] C. Gonzalez, F. Flores, and J. Ortega, Soft phonon, dynamical fluctuations, and a reversible phase transition: Indium chains on silicon, Phys. Rev. Lett. **96**, 136101 (2006).

[23] M. Hashimoto, Y. Fukaya, A. Kawasuso, and A. Ichimiya, Quasi-one-dimensional in atomic chains on Si(111) at low temperature studied by reflection highenergy positron diffraction and scanning tunneling microscopy, Appl. Surf. Sci. **254**, 7733 (2008).

[24] Y. Fukaya, M. Hashimoto, A. Kawasuso, and A. Ichimiya, Surface structure of Si(111)-(82)–In determined by reflection high-energy positron diffraction, Surf. Sci. **602**, 2448 (2008).

[25] S. Chandola, K. Hinrichs, M. Gensch, N. Esser, S. Wippermann, W. G. Schmidt, F. Bechstedt, K. Fleischer, and J. F. McGilp, Structure of Si(111)-In Nanowires Determined From the Midinfrared Optical Response, Phys. Rev. Lett. **102**, 226805 (2009).

[26] C. González, J. Guo, J. Ortega, F. Flores, and H. H. Weitering, Mechanism of the Band Gap Opening Across the Order-

Disorder Transition of Si(111)(4×1)-In, Phys. Rev. Lett. **102**, 115501 (2009).

[27] S. Wippermann and W. G. Schmidt, Entropy Explains Metal-Insulator Transition of the Si(111)-In Nanowire Array, Phys. Rev. Lett. **105**, 126102 (2010).

[28] A. A. Stekolnikov, K. Seino, F. Bechstedt, S. Wippermann, W. G. Schmidt, A. Calzolari, and M. Buongiorno Nardelli, Hexagon versus Trimer Formation in In Nanowires on Si(111): Energetics and Quantum Conductance, Phys. Rev. Lett. **98**, 026105 (2007).

[29] J.-H. Cho and J.-Y. Lee, First-principles calculation of the atomic structure of one-dimensional indium chains on Si(111): Convergence to a metastable structure, Phys. Rev. B **76**, 033405 (2007).

[30] H.-J. Kim and J.-H. Cho, Driving Force of Phase Transition in Indium Nanowires on Si(111), Phys. Rev. Lett. **110**, 116801 (2013).

[31] U. Gerstmann, N. J. Vollmers, A. Lücke, M. Babilon, and W. G. Schmidt, Rashba splitting and relativistic energy shifts in In/Si(111) nanowires, Phys. Rev. B **89**, 165431 (2014).

[32] F. Klasing, T. Frigge, B. Hafke, B. Krenzer, S. Wall, A. Hanisch-Blicharski, and M. Horn-von Hoegen, Hysteresis proves that the In/Si(111) (8×2) to (4×1) phase transition is first-order, Phys. Rev. B **89**, 121107 (2014).

[33] G. Lee, J. Guo, and E. W. Plummer, Real-Space Observation of Nanoscale Inhomogeneities and Fluctuations in a Phase Transition of a Surface Quasi-One-Dimensional System: In/Si(111), Phys. Rev. Lett. **95**, 116103 (2005).

[34] G. Lee, S.-Y. Yu, H. Kim, and J.-Y. Koo, Defect-induced perturbation on Si(111)4×1-In: Period-doubling modulation and its origin, Phys. Rev. B **70**, 121304(R) (2004).

[35] S. V. Ryjkov, T. Nagao, V. G. Lifshits, and S. Hasegawa, Phase transition and stability of Si(111)-8×2-In surface phase at low temperatures, Surf. Sci. **488**, 15 (2001).

[36] G. Lee, S.-Y. Yu, H. Shim, W. Lee, and J.-Y. Koo, Roles of defects induced by hydrogen and oxygen on the structural phase transition of Si(111)4×1-In, Phys. Rev. B **80**, 075411 (2009).

[37] S. Wall, B. Krenzer, S. Wippermann, S. Sanna, F. Klasing, A. Hanisch-Blicharski, M. Kammler, W. G. Schmidt, and M. Horn-von Hoegen, Atomistic Picture of Charge Density Wave Formation at Surfaces, Phys. Rev. Lett. **109**, 186101 (2012).

[38] W. G. Schmidt, M. Babilon, C. Thierfelder, S. Sanna, and S. Wippermann, Influence of Na adsorption on the quantum conductance and metal-insulator transition of the In-Si(111)(4×1)–(8×2) nanowire array, Phys. Rev. B **84**, 115416 (2011).

[39] H. Zhang, F. Ming, H.-J. Kim, H. Zhu, Q. Zhang, H. H. Weitering, X. Xiao, C. Zeng, J.-H. Cho, and Z. Zhang, Stabilization and Manipulation of Electronically Phase-Separated Ground States in Defective Indium Atom Wires on Silicon, Phys. Rev. Lett. **113**, 196802 (2014).

[40] K. Fleischer, S. Chandola, N. Esser, W. Richter, and J. F. McGilp, Surface phonons of the Si(111):In-(4×1) and (8×2) phases, Phys. Rev. B **76**, 205406 (2007).

[41] N. Esser, M. Köpp, P. Haier, and W. Richter, Vibrational-modes of epitaxial monolayer adsorbates on semiconductor surfaces studied by Raman-scattering, J. Electron Spectrosc. **64-65**, 85 (1993).

[42] K. Hinrichs, A. Schierhorn, P. Haier, N. Esser, W. Richter, and J. Sahm, Surface Phonons of InP(110) Studied by Raman Spectroscopy, Phys. Rev. Lett. **79**, 1094 (1997).

[43] M. Hünermann, J. Geurts, and W. Richter, Observation of Interface Phonons by Light Scattering from Epitaxial Sb Monolayers on III-V Semiconductors, Phys. Rev. Lett. **66**, 640 (1991).

[44] Edited by M. Cardona and G. Güntherodt, Raman scattering from surface phonons, in *Light Scattering in Solids* (Springer, Berlin, 2000), Vol. viii.

[45] N. Esser, K. Hinrichs, J. R. Power, W. Richter, and J. Fritsch, Surface vibrational modes of Sb-terminated (110) surfaces of III-V semiconductors investigated by Raman spectroscopy, Phys. Rev. B **66**, 075330 (2002).

[46] P. V. Santos, N. Esser, M. Cardona, W. G. Schmidt, and F. Bechstedt, Optical properties of Sb-terminated GaAs and InP (110) surfaces, Phys. Rev. B **52**, 12158 (1995).

[47] J. Räthel, E. Speiser, N. Esser, U. Bass, S. Meyer, J. Schäfer, and J. Geurts, Surface phonons of Ge(001) and their correlation with the p(2×1) and c(4×2) reconstruction as shown by Raman spectroscopy, Phys. Rev. B **86**, 035312 (2012).

[48] M. Liebhaber, U. Bass, P. Bayersdorfer, J. Geurts, E. Speiser, J. Räthel, A. Baumann, S. Chandola, and N. Esser, Surface phonons of the Si(111)-(7×7) reconstruction observed by Raman spectroscopy, Phys. Rev. B **89**, 045313 (2014).

[49] K. Fleischer, S. Chandola, N. Esser, W. Richter, and J. F. McGilp, Reflectance anisotropy spectroscopy of Si(111)-(4×1)-In, Phys. Status Solidi A **188**, 1411 (2001).

[50] M. Cardona , *Light Scattering in Solids* (Springer, Berlin, 1982), Vol. ii.

[51] A. Compaan and H. J. Trodahl, Resonance Raman scattering in Si at elevated temperatures, Phys. Rev. B **29**, 793 (1984).

[52] S. Wippermann and W. G. Schmidt, Optical anisotropy of the In/Si(111)(4×1)/(8×2) nanowire array, Surf. Sci. **603**, 247 (2009).

[53] D. M. Ceperley and B. J. Alder, Ground State of the Electron Gas by a Stochastic Method, Phys. Rev. Lett. **45**, 566 (1980).

[54] G. Kresse and J. Furthmüller, Efficiency of ab-initio total energy calculations for metals and semiconductors using a plane-wave basis set, Comput. Mater. Sci. **6**, 15 (1996).

[55] W. G. Schmidt, F. Bechstedt, and G. P. Srivastava, III-V(110) surface dynamics from *ab initio* frozen-phonon approach, Phys. Rev. B **52**, 2001 (1995).

[56] S. S. Lee, J. R. Ahn, N. D. Kim, J. H. Min, C. G. Hwang, J. W. Chung, H. W. Yeom, S. V. Ryjkov, and S. Hasegawa, Adsorbate-Induced Pinning of a Charge-density Wave in a Quasi-1D Metallic Chains: Na on the In/Si(111)-(4×1) surface, Phys. Rev. Lett. **88**, 196401 (2002).